



Experimental and numerical studies on the behavior of thin aluminum plates subjected to impact by blunt- and hemispherical-nosed projectiles

N.K. Gupta*, M.A. Iqbal, G.S. Sekhon

Department of Applied Mechanics, Indian Institute of Technology Delhi, Hauz Khas, New Delhi 110016, India

Received 3 February 2005; received in revised form 16 June 2005; accepted 23 June 2005

Available online 22 August 2005

Abstract

Experiments were conducted on aluminum plates of 1 mm thickness by using a gas gun and projectiles with blunt and hemispherical noses. Target plate was impacted with varying impact velocity. Impact and residual velocities of the projectile were measured. Ballistic limit velocity was found to be higher for hemispherical projectiles than that for blunt projectiles. Effect of nose shape on the deformation of the plate was also studied. Numerical simulations of the impact were conducted by using an explicit finite element code (ABAQUS). Johnson–Cook elasto-viscoplastic model available in the code was used to carryout the analysis. Material property tests were carried out with the help of smooth and notched tensile test specimens. Results obtained from finite element simulations were compared with those of experiments. Good correlation was found between the two. It was observed that the element size significantly affects the numerical results; therefore a sufficiently refined mesh was used. Adaptive meshing was found helpful especially in the case of impact by a hemispherical projectile.

© 2005 Elsevier Ltd. All rights reserved.

Keywords: Experiments; Numerical simulation; Penetration; Johnson–Cook model; Nose shape

*Corresponding author. Tel.: +91 11 2659 1178; fax: +91 11 2658 1119.
E-mail address: nkgupta@am.iitd.ernet.in (N.K. Gupta).

Nomenclature

D	deformation
E	energy
M	mass
P	perforation
V	velocity of projectile

Subscripts

abs	absorbed
d	drop
f	full/final
i	initial value
max	maximum
pl	plug
r	residual value

1. Introduction

Due to the complex nature of the problem, structural impact is still not fully understood, despite a large number of studies that have been carried out in the last few decades.

Corran et al. [1] investigated the effect of projectile mass, nose shape and hardness on penetration of steel and aluminum alloy plates of varying thickness. They used blunt and cylindro-conical projectiles and observed that the ballistic limit of the plate changes with change of projectile mass and nose shape.

Levy and Goldsmith [2] used blunt, spherical and conical projectiles and measured impact load, permanent deflection and strain in aluminum and mild steel plates. They observed that an increase in the projectile mass results in a decrease of the ballistic limit.

Ipson and Recht [3] found that blunt projectiles penetrated the target more efficiently than conical projectiles when the thickness of target was moderate. In the case of thin and thick targets, however, an opposite trend was observed.

Investigations carried out by Wingrove [4] on aluminum alloy targets suggested that blunt projectiles can penetrate the target more efficiently than either the hemispherical- or ogive-nosed penetrators, if the ratio of target thickness to projectile diameter is less than one.

Othe et al. [5] found that conical projectiles are efficient penetrators. As their nose angle is decreased, the perforation resistance of the target tends to drop. The critical perforation energies were found to be equal in the case of blunt and hemispherical projectiles.

Camacho and Ortiz [6] carried out finite element simulation of projectile impact. They used adaptive meshing to avoid problems of mesh distortion and evolving contact. They reported good agreement between the computational and experimental results for the case of impact of aluminum plates by conical-nosed projectiles.

Borvik et al. [7] carried out experimental and numerical investigation on impact of steel plates with blunt nose projectiles. They used a finite element model and predicted the influence of various parameters such as material damage, temperature and strain rate. They found that element size is a vital parameter in numerical simulation because results are significantly improved by refining the mesh.

Borvik et al. [8,9] further studied the impact behavior of steel plates when struck by blunt, hemispherical and conical projectiles. They found from experiments that blunt projectiles were more efficient penetrators than hemispherical and conical projectiles at low velocities. However at higher impact velocities, conical projectiles required less energy to perforate the target. Close agreement was found between experimental and corresponding finite element results. It was shown that adaptive meshing is desirable in 2D simulations of impact by conical and hemispherical projectiles. They also found good agreement between adaptive simulations and experimental results.

The above discussion shows that even though different aspects of the impact problem have been studied in previous experimental, analytical and numerical investigations, yet the problem of projectile impact on metallic plates continues to attract research attention on account of the involvement of a large number of factors including material parameters, target and projectile geometry, boundary conditions and velocity of impact. Variations in the above factors have profound influence on the deformation behavior of the target plate. Different researchers have often used different impact conditions and obtained conflicting results. In the present experimental program, projectiles of two different nose shapes have been impacted onto 1 mm-thick aluminum plates. Impact and residual velocities have been measured and energy absorbed by the plates has been calculated. Finite element simulation of the impact situation has also been carried out by using an explicit finite element code namely, ABAQUS version 6.3 [10]. Adaptive meshing has been found helpful. Mesh density is found to be a significant parameter affecting accuracy of the computational results. As the size of the element in the “influence zone” was reduced, improved results were obtained. Results of numerical simulations are discussed and compared with those of experiment.

2. Experimental investigation

The present experimental study was carried out with the help of a gas gun comprising of a pressure chamber, a release valve, a projectile chamber and a changeable barrel (Fig. 1). Impact velocity of the projectile was measured with the help of a photo gate type arrangement comprising of three infrared light emitting diodes and three infrared light sensing photodiodes. Residual velocity of the projectile was measured with the help of two sets of aluminum foil screens of 6 μm thickness, placed behind the target plate. Data was recorded by means of an electronic counter timer (Apollo 100) and a digital oscilloscope (Gould 1604). Projectiles were made of EN-24 steel, oil quenched to Rockwell hardness R_c of 47–52. Hollow projectiles of 2.44 mm wall thickness (Fig. 2) were fired at varying impact velocity. The mass of the blunt projectile was 52.5 g, while the hemispherical projectile weighed 47.0 g. Circular target plates of diameter 255 mm were fixed to a thick mounting plate by means of 16 bolts arranged on a 230 mm diameter pitch circle. The free flight of the projectile was kept small to ensure normal impact. After perforation, the projectile,

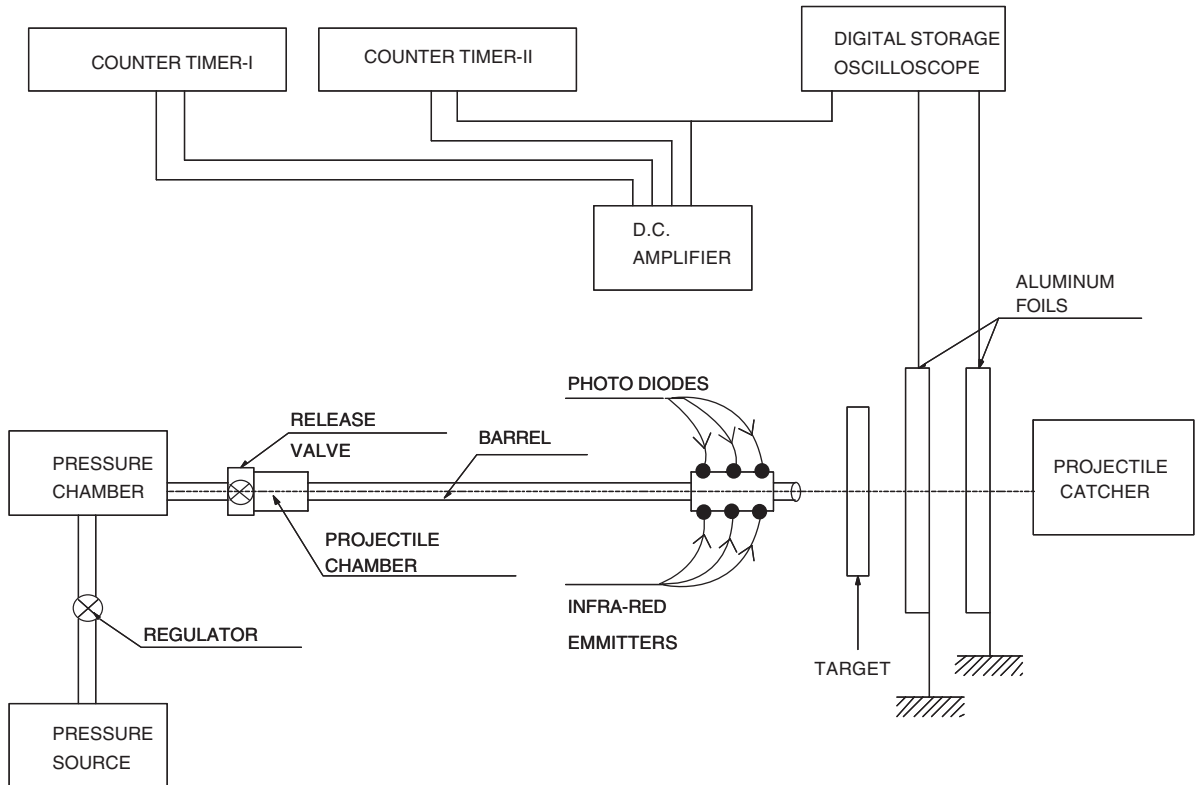


Fig. 1. Schematic diagram of the experimental setup.

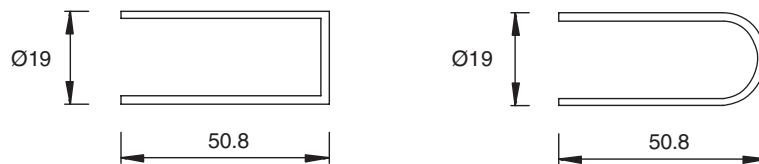


Fig. 2. Geometry of the blunt- and hemispherical-nosed projectiles.

and the plug if formed, were recovered from a wooden catcher positioned behind the residual velocity measurement apparatus. The catcher was filled with cotton rag to avoid damaging the projectile. Deformed profile of the target plate was measured with the help of a dial gauge system.

3. Experimental results

The purpose of the present experimental study was to observe the response of 1100-H12 aluminum plates to impact by blunt and hemispherical projectiles. All variables except the initial velocity of the projectile were kept constant during successive tests. Deformed profile of the plates

was studied and it was observed that the blunt projectile requires less energy to perforate the target as compared to the projectile with a hemispherical nose. Kinetic energy of both types of the projectile is dissipated in local and diffuse deformation. The diffuse (global) deformation, however, is observed to be smaller in case of the blunt projectile. When the blunt projectile hits the target, a circular plug of diameter equal to the diameter of the projectile is sheared out in a clean cut. The material in front of the projectile gets accelerated and narrow shear bands are formed characterised by large strain and strain rate. The adiabatic temperature rise, however, is not significant. Hemispherical projectiles, on the other hand, deform the targets mainly by ductile hole enlargement. The material in front of the projectile is pushed forward. There is thinning of a portion of material and formation of small petals. A thin plug of considerably smaller diameter than the diameter of the projectile “just” gets fully separated from the plate. (The plug remains attached to one of the petals.) This phenomenon was also observed by Levy and Goldsmith [2]. The diameter of the perforated hole was found to be smaller than that of the projectile, due to elastic recovery. Deformed target plates and the projectiles are shown in Fig. 3. Fig. 4 shows the measured impact and residual velocity curves for both types of the projectile. At lower impact velocities, the velocity drop (difference between the impact and residual velocities) is greater in case of the hemispherical projectile. But as the impact velocity is increased, the velocity drop curves of both the projectiles overlap. Experimental results on the effect of impact velocity V_i on the residual velocity of the projectile V_r , velocity drop $V_d = V_i - V_r$, weight of the plug M_{pl} , energy absorbed by the target E_{abs} , and maximum deformation of the target D_{max} are shown in Table 1. It is observed that as the impact velocity is increased, the velocity drop of the projectiles decreases. It is also found that the maximum deformation of the target plate decreases with increase of impact velocity. At low impact velocity bending of the plate is greater and the same is reduced with increasing impact velocity. Consequently velocities drop of the projectile decreases at higher velocities of impact. No significant difference in the masses of plugs formed by blunt projectile at different velocities is obtained. In case of the hemispherical projectile also, the size of the plug is more or less constant for all impact velocities. However hemispherical projectiles cause more intense diffuse deformation of the target plate than the blunt projectile. No sign of projectile deformation was observed in any test. Ballistic limit velocity for both the projectiles has been obtained from the experiments (Table 2). The ballistic limit is higher in the case of the

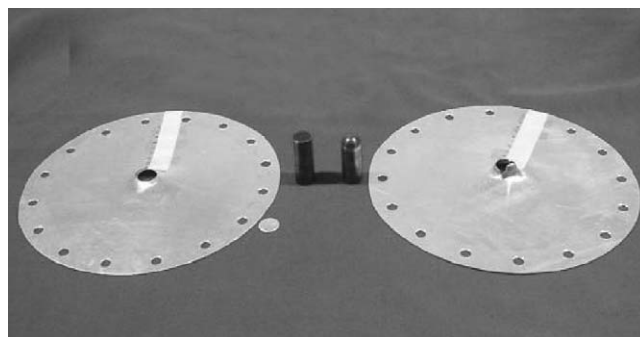


Fig. 3. Photographs of the projectiles and the deformed specimens.

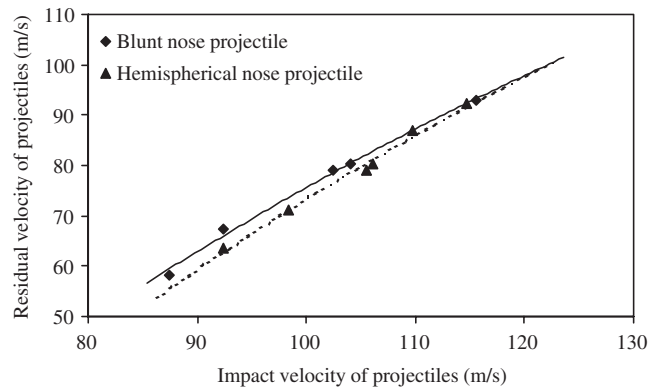


Fig. 4. Variation of residual velocity with impact velocity.

Table 1

Observed values of impact velocity V_i , residual velocity V_r , velocity Drop V_d , mass of the plug M_{pl} , energy absorbed by the target E_{abs} , and maximum deformation of the target D_{max}

Test	V_i (m/s)	V_r (m/s)	V_d (m/s)	M_{pl} (gms)	E_{abs} (joule)	D_{max} (mm)
<i>Blunt projectile, mass = 52.5 g</i>						
1	115.6	92.9	22.7	1.0	124.2	8.9
2	104.0	80.2	23.8	1.5	115.0	8.9
3	102.5	79.2	23.3	1.0	111.1	10.1
4	92.5	67.5	25.0	0.9	105.0	11.0
5	87.5	58.3	29.2	1.0	111.7	11.4
6	73.9	43.8	30.1	—	93.0	11.8
<i>Hemispherical projectile, mass = 47.0 g</i>						
1	114.7	92.3	22.4	—	109.0	12.2
2	109.7	86.8	22.9	—	105.7	13.3
3	106.1	80.1	26.0	—	113.7	14.1
4	105.5	79.0	26.5	—	114.8	14.3
5	98.3	71.0	27.3	—	108.6	15.1
6	92.3	63.5	28.8	—	105.4	15.8

Table 2

Observed and predicted ballistic limit velocity for blunt as well as hemispherical nosed projectiles

	Experimental (m/s)	Numerical (m/s)
Blunt projectile	61.3	66.7
Hemispherical projectile	85.9	96.3

hemispherical projectile than in the case of the blunt projectile. It indicates that the proportion of energy absorbed in diffuse deformation is more in the hemispherical projectile case than in the blunt projectile case.

4. Material modeling

The quality of the material model is a key factor affecting the accuracy of results of a finite element simulation, especially of the impact phenomenon. Two different types of material model are generally used in numerical simulations. One of these represents plastic flow and the other fracture of the material. A number of models of each type have been proposed in the past, some of which involve several parameters. Due to difficulties in the determination of the material parameters from material tests, simpler models are preferred. The ABAQUS 6.3 code [10] has an inbuilt option of the material model proposed by Johnson and Cook [11]. The latter is quite suited to problems of impact and penetration. It allows for linear thermo-elasticity, yielding, plastic flow, isotropic strain hardening, strain rate effect, and softening due to adiabatic heating and damage. According to the Johnson and Cook, the equivalent stress $\bar{\sigma}$ may be expressed as follows:

$$\bar{\sigma} = [A + B(\bar{\epsilon}^{pl})^n] \left[1 + C \ln \left(\frac{\dot{\bar{\epsilon}}^{pl}}{\dot{\epsilon}_0} \right) \right] (1 - \hat{T}^m), \quad (1)$$

where A , B , C , n , and m are material parameters, $\bar{\epsilon}^{pl}$ is the equivalent plastic strain, $\dot{\bar{\epsilon}}^{pl}$ is equivalent plastic strain rate, $\dot{\epsilon}_0$ is a reference strain rate, and \hat{T} is the non-dimensional temperature defined as below.

$$\hat{T} = (T - T_0)/(T_{\text{melt}} - T_0) \quad T_0 \leq T \leq T_{\text{melt}}, \quad (2)$$

where T is the current temperature, T_{melt} is the melting point temperature, and T_0 is the room temperature.

The fracture model proposed by Johnson and Cook [12] takes into account the effect of stress triaxiality, strain rate, and temperature on the equivalent failure strain. The failure criterion is based on the value of the equivalent plastic strain at element integration points. Failure is assumed to occur when the damage parameter D exceeds unity [10]. The damage parameter, D , is defined as follows:

$$D = \sum \left(\frac{\Delta \bar{\epsilon}^{pl}}{\bar{\epsilon}_f^{pl}} \right), \quad (3)$$

where $\Delta \bar{\epsilon}^{pl}$ is an increment of the equivalent plastic strain, $\bar{\epsilon}_f^{pl}$ is the equivalent strain at failure, and the summation is performed over all increments of deformation. The strain at failure, $\bar{\epsilon}_f^{pl}$, is assumed to be dependent on a non-dimensional plastic strain rate, $\dot{\bar{\epsilon}}^{pl}/\dot{\epsilon}_0$, a dimension-less pressure–deviatoric stress ratio, $\sigma_m/\bar{\sigma}$ (where σ_m is the mean stress), and the non-dimensional temperature, \hat{T} , defined earlier. The dependencies are assumed separable and are of the form given below.

$$\bar{\epsilon}_f^{pl} = \left[D_1 + D_2 \exp \left(D_3 \frac{\sigma_m}{\bar{\sigma}} \right) \right] \left[1 + D_4 \ln \left(\frac{\dot{\bar{\epsilon}}^{pl}}{\dot{\epsilon}_0} \right) \right] (1 + D_5 \hat{T}), \quad (4)$$

where D_1 – D_5 are material constants. When this failure criterion is met, the deviatoric components of stress are set to zero and remain zero during the rest of the analysis. The “element kill”

algorithm available in the software [10] has been used to delete the failed elements from the mesh. It ensures that the mean stress in killed elements is zero during subsequent analysis.

Material parameters for the test material were found from mechanical tests. Round specimens of the test material Aluminum (1100-H12) were prepared (Fig. 5a). Uni-axial tensile tests were carried out on a Zwick Z250/SN5A universal testing machine at a fixed strain rate of $4.16 \times 10^{-4} \text{ s}^{-1}$. Values of modulus of elasticity, Poisson's ratio and yield stress were determined. Diameter reduction was observed till fracture using a digital Vernier caliper of 0.01 mm least count. True strain in the necked portion was obtained from the following expression:

$$\bar{\varepsilon}^{\text{pl}} = 2 \ln(d_0/d), \quad (5)$$

where, d_0 is the initial diameter and d is the current diameter of the specimen. True stress was found as the ratio F/A , where F is the measured force and A is the actual area of cross section. The stress in the specimen is practically uniaxial before the onset of necking. However after the necking starts, the stress state becomes three-dimensional. Bridgman correction [13] was applied to the measured true stress and the equivalent stress $\bar{\sigma}$ was calculated by using the following expression:

$$\frac{\bar{\sigma}_x}{\bar{\sigma}} = \left(1 + \frac{2R}{a}\right) \ln\left(1 + \frac{a}{2R}\right), \quad (6)$$

where $\bar{\sigma}_x$ is the measured true stress, R is the radius of curvature of the neck and a is the current radius of specimen in the necked region. During the experiments, reduction of specimen diameter was measured but the radius of curvature was not obtained. Instead the ratio a/R was acquired by using the empirical expression proposed by Le Roy et al. [14];

$$\frac{a}{R} = \begin{cases} 0 & \text{for } \varepsilon \leq \varepsilon_u, \\ 1.11(\varepsilon - \varepsilon_u) & \text{for } \varepsilon > \varepsilon_u, \end{cases} \quad (7)$$

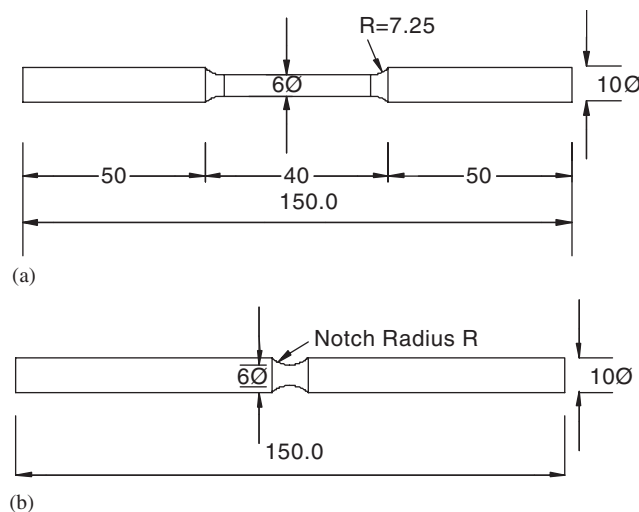


Fig. 5. Geometry of the tensile test specimens.

where ε_u and ε are ultimate and actual true strains of the specimen. The factor 1.11 in the above expression, although validated for steel, was considered valid for aluminum also. The corrected true stress–true strain curve is shown in Fig. 6. The above stress–strain curve was next used to compute the values of the strain hardening constants B and n by using the least-squares method. The Johnson–Cook constants, C and m in the next two brackets of equivalent stress expression (Eq. (4)) were taken from the work of Borvik et al. [15]. (It may be mentioned that the aluminum alloy used by Borvik et al. was comparatively richer in magnesium and they used a slightly modified version of Johnson–Cook constitutive relation). Tests were also performed on notched specimens (Fig. 5b) of three different notch radii, namely 2, 0.8 and 0.4 mm. An artificial notch produces an initial triaxiality different from that in the case of a smooth specimen where triaxiality is initiated only after the commencement of necking. Bridgman’s relationship was used to correlate initial notch radius R and maximum stress triaxiality ratio σ_{\max}^* .

$$\sigma_{\max}^* = \frac{1}{3} + \ln\left(1 + \frac{a}{2R}\right). \quad (8)$$

The triaxiality ratios obtained from the above expression for different specimens are listed in Table 3. Measured values of fracture strain (Fig. 7) were used to obtain the parameters D_1 , D_2 , D_3 , (Eq. (4)). The value of D_4 that expresses the strain rate effect on the equivalent fracture strain has been taken from the work of Borvik et al. [15]. This is an approximation since the aluminum alloy used in the present study is not identical to that used by Borvik et al. [15]. Also they used a slightly

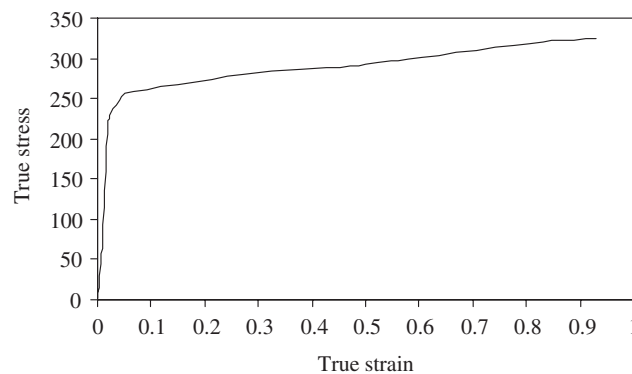


Fig. 6. True stress–strain curve.

Table 3

Measured values of fracture strain as a function of stress triaxiality ratio

Fracture strain, $\varepsilon_f^{\text{pl}}$	Triaxiality ratio, σ_{\max}^*
0.929	0.333
0.497	0.893
0.364	1.389
0.197	1.891

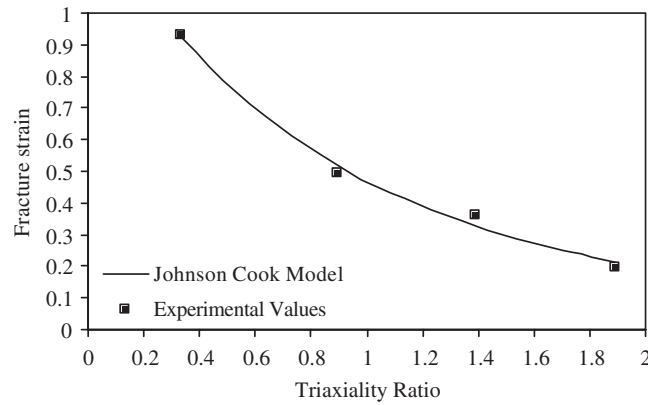


Fig. 7. Effect of triaxiality ratio on fracture strain.

Table 4
Material parameters for the tests specimens

Modulus of elasticity, E (N/mm ²)	65.762×10^3
Poisson's ratio, ν	0.3
Density, ρ (kg/m ³)	2700
Yield stress, A (N/mm ²)	148.361
B (N/mm ²)	345.513
n	0.183
C	0.001
Reference strain rate, $\dot{\epsilon}_0$ (1/s)	1.0
m	0.859
T_{melt} (K)	893
T_0 (K)	293
Specific heat, C_p (J/kg K)	920
Inelastic heat fraction, α	0.9
D_1	0.071
D_2	1.248
D_3	-1.142
D_4	0.147
D_5	0.0

modified version of the Johnson–Cook model to express the strain rate effect. Since the target plates are thin and the velocity of the projectiles is low, adiabatic temperature rise was not considered significant. This assumption was validated by carrying out finite element simulation to estimate adiabatic temperature rise during impact. The maximum temperature rise was found to be 279 and 247 °C in the case of blunt and hemispherical projectiles, respectively. The temperature rise is too low to cause significant softening of the material. Therefore the parameter D_5 was considered to be vanishingly small. Borvik et al. [7,9,16] carried out numerical simulations of perforation problems on 8 and 12 mm-thick Weldox steel plates with projectiles of different nose shape. They also reported that the effect of adiabatic heating was of minor importance. The different material parameters used in the present study are listed in Table 4.

5. Numerical Investigation

Most of the previous numerical studies of structural impact have been performed using the code LS-DYNA. In the present study the ABAQUS 6.3 [10] code has been used. The code includes a general purpose finite element program (ABAQUS standard), and an explicit finite element program (ABAQUS explicit). The latter uses a central difference time integration rule to efficiently analyse incremental deformation. An explicit central difference operator satisfies the dynamic equilibrium equations at the beginning of the increment, t . The accelerations calculated at time t are used to advance the velocity solution to time $t + \Delta t/2$ and the displacement solution to time $t + \Delta t$.

An objective of the present study was to find whether the explicit finite element scheme of ABAQUS 6.3 could be used in conjunction with the Johnson–Cook plasticity model to solve the penetration problems involving fracture. To achieve the objective, an axisymmetric geometric model was created by using the preprocessing module of the ABAQUS code. The target plate was modeled as a deformable body and material properties were assigned to it as discussed earlier. The bullet was modeled as a rigid body. A single node reference point was used to assign mass and initial velocity. Four noded axisymmetric elements and single point integration were used during the analysis. The mesh was refined in the impact zone. The mesh density was reduced as the distance from the impact area increased. A large number of elements were taken in the thickness direction. Care was also taken to maintain correct aspect ratio in the grid especially in and around the impact zone where the aspect ratio of the elements was maintained close to unity. The aspect ratio was allowed to increase towards the periphery of the plate. Surface to surface contact between the bullet and the plate was modeled by using a kinematic contact algorithm. The bullet was considered as the master surface and the contact surface of the plate as the slave surface. The effect of friction between projectile and target was neglected. To verify the forgoing assumption a finite element solution of the problem was obtained using two different values of the assumed dynamic coefficient of friction namely 0 and 0.05 between the bullet and the target plate. No significant difference in the computational results was observed.

6. Choice of mesh

The proposed finite element model of the bullet and the plate prior to impact is shown in the Fig. 8. The total number of elements in the mesh was 9108 in the blunt projectile case. There were 18 elements in the thickness direction of the plate. For the case of impact by the hemispherical projectile, the number of elements needed for solution convergence and avoidance of excessive element distortion was 13 590. As many as 30 elements were needed in the thickness direction of the plate. Adaptive meshing was also employed in the case of impact by the hemispherical projectile, primarily to avoid problems of excessive distortion of elements in the mesh. (The adaptive meshing available in ABAQUS does not change the total number of elements or nodal connectivity). The so-called Lagrangian adaptive meshing was used in the region of the target plate directly in front of the projectile and equal to its radius. Thirty mesh sweeps were performed at each increment. Excessive distortion of some elements did occur during finite element analysis of impact by blunt projectiles. However this happened at low mesh densities. When sufficiently

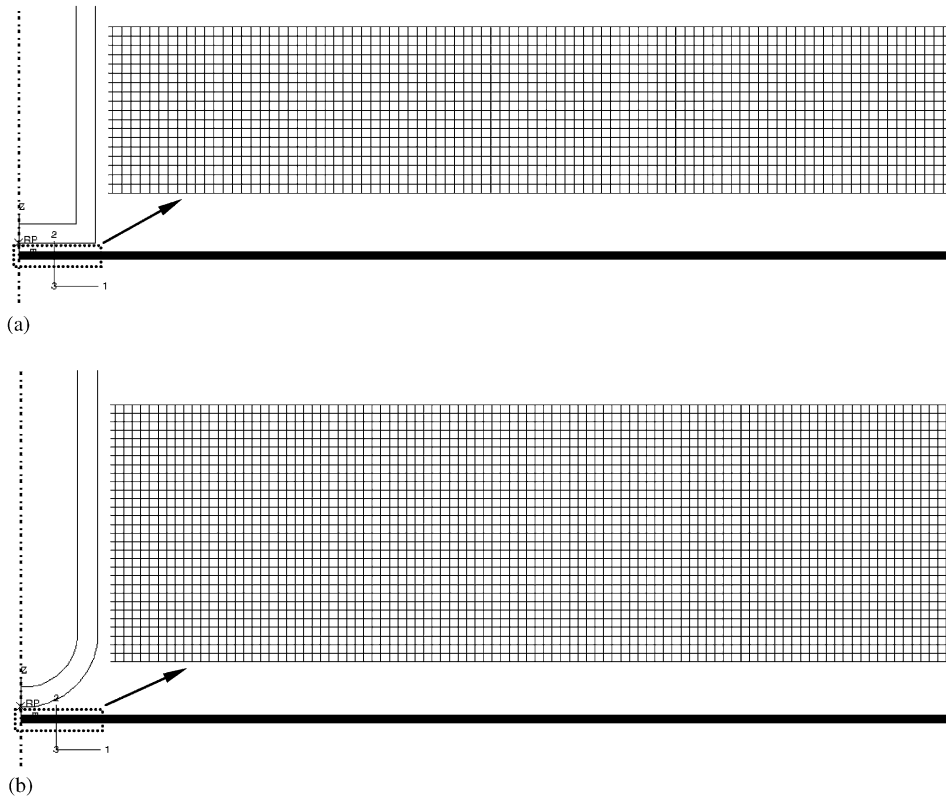


Fig. 8. Finite element mesh.

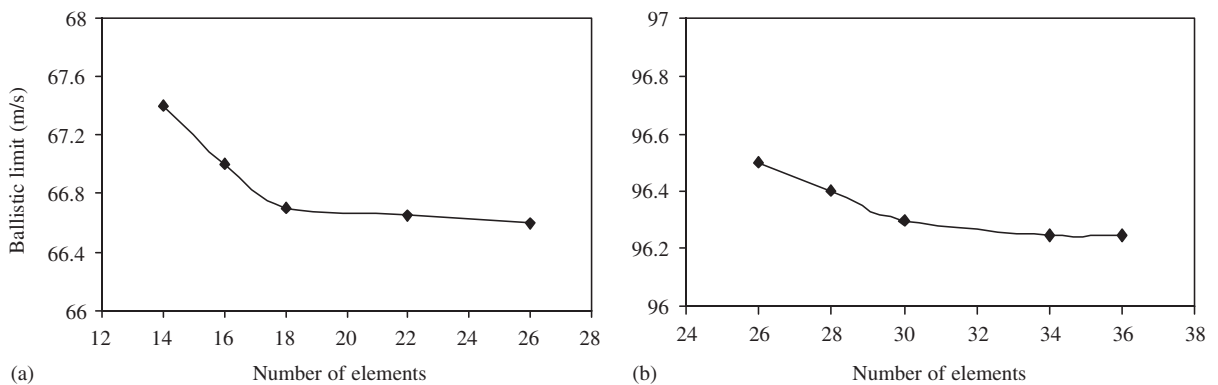


Fig. 9. Variation of the ballistic limit with number of elements across the thickness of the target impacted by projectiles: (a) blunt-nosed, (b) hemispherical-nosed.

fine mesh was used, the numerical difficulty associated with excessive distortion was overcome. Solution accuracy was tested by carrying out computations of ballistic limit using variable mesh density (Fig. 9).

7. Computational results

Simulations of impact of aluminum plates by blunt- and hemispherical-nosed projectiles were carried out at different velocities of impact. Table 5 lists the predictions of the residual projectile velocity, perforation time and target deformation as a result of impact. Experimentally and numerically obtained impact and residual velocities are compared in Figs. 10 and 11. The maximum deviation between the actual and predicted values of the residual velocities was 4.5% and 8.7% corresponding to hemispherical and blunt projectiles, respectively. It is also found that velocity drop of the projectile decreases with increase of the impact velocity (Figs. 12 and 13). In case of blunt projectiles, the predicted velocity drop is higher than the actual at lower velocities of impact. At higher impact velocities, an opposite trend is observed. The deviation between predicted and actual velocity drops was found to be smaller in the case of impact with hemispherical projectiles. Ballistic limit velocity for both the projectiles has been measured from numerical simulations and compared with experimental values in Table 2. It is found that the predicted values of the ballistic limit are 8.0% and 10.7% higher than the actual values in the case of blunt and hemispherical projectiles, respectively. It is quite clear from both experimental as well as numerical results that hemispherical projectiles are less effective to perforate the targets. Borvik et al. [8,9] observed that ballistic limit velocity of the target plate is severely affected by the nose shape of the projectiles. They found from experiments that for 12 mm-thick steel plates the ballistic limit velocity for hemispherical and conical projectiles was about 300 m/s while for blunt projectile it was 185 m/s.

The deformed plate profiles are shown in Fig. 14. It is observed that the blunt projectile shears out a plug of diameter equal to that of the projectile. The deformation is highly localised. On the other hand, the hemispherical projectile pushes the material in front of itself, stretches the target material and removes a plug that is smaller in diameter than that of the projectile. The hemispherical projectile causes more prominent bending of the target plate as compared to the

Table 5

Predicted values of impact velocity V_i , residual velocity V_r , velocity drop V_d , velocity of the Plug V_{pl} , energy absorbed by the target E_{abs} , full perforation time of the Target P_f , and maximum deformation of the target D_{max}

Test	V_i (m/s)	V_r (m/s)	V_d (m/s)	V_{pl} (m/s)	E_{abs} (J)	P_f (s)	D_{max} (mm)
<i>Blunt projectile, mass = 52.5 g</i>							
1	115.6	98.6	17.0	106.2	95.5	7.0e-4	8.5
2	104.0	83.9	20.1	91.7	99.1	8.0e-4	8.5
3	102.5	82.5	20.0	90.2	97.1	8.0e-4	9.0
4	92.5	63.3	29.2	70.5	119.4	8.5e-4	9.8
5	87.5	53.2	34.4	63.4	126.9	8.5e-4	10.1
6	73.9	40.6	33.3	49.4	100.0	9.0e-4	10.5
<i>Hemispherical projectile, mass = 47.0 g</i>							
1	114.7	96.6	18.1	110.1	89.8	7.0e-4	11.9
2	109.7	89.7	20.0	103.4	93.7	7.5e-4	13.2
3	106.1	83.8	22.3	98.6	99.5	8.0e-4	13.6
4	105.5	82.4	23.1	98.0	102.0	8.0e-4	14.2
5	98.3	73.5	24.8	89.1	100.1	8.5e-4	14.3

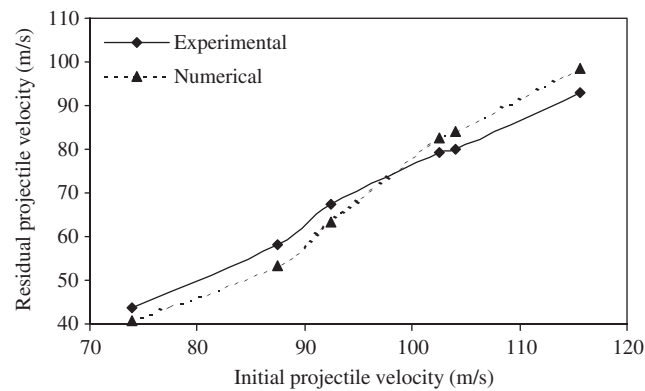


Fig. 10. Variation of residual velocity with impact velocity (blunt-nosed projectile case).

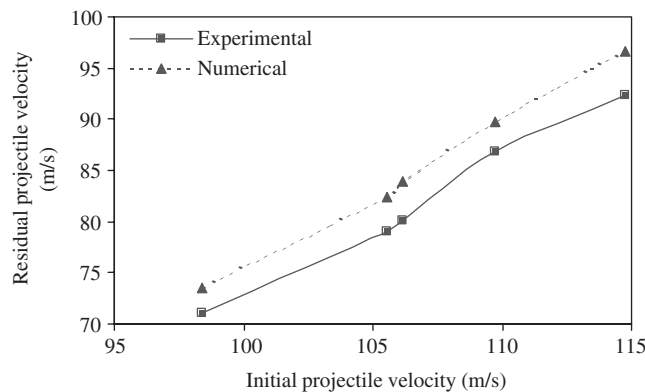


Fig. 11. Variation of residual velocity with impact velocity (hemispherical-nosed projectile case).

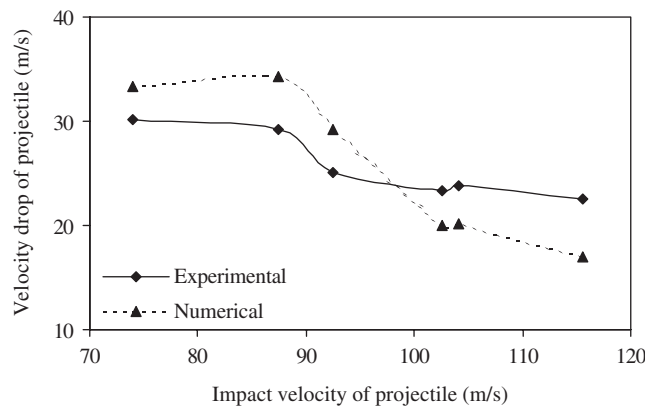


Fig. 12. Variation of velocity drop with impact velocity (blunt-nosed projectile case).

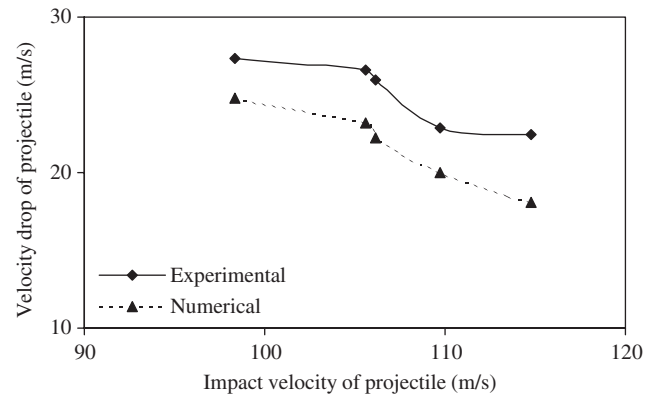


Fig. 13. Variation of velocity drop with impact velocity (hemispherical-nosed projectile case).

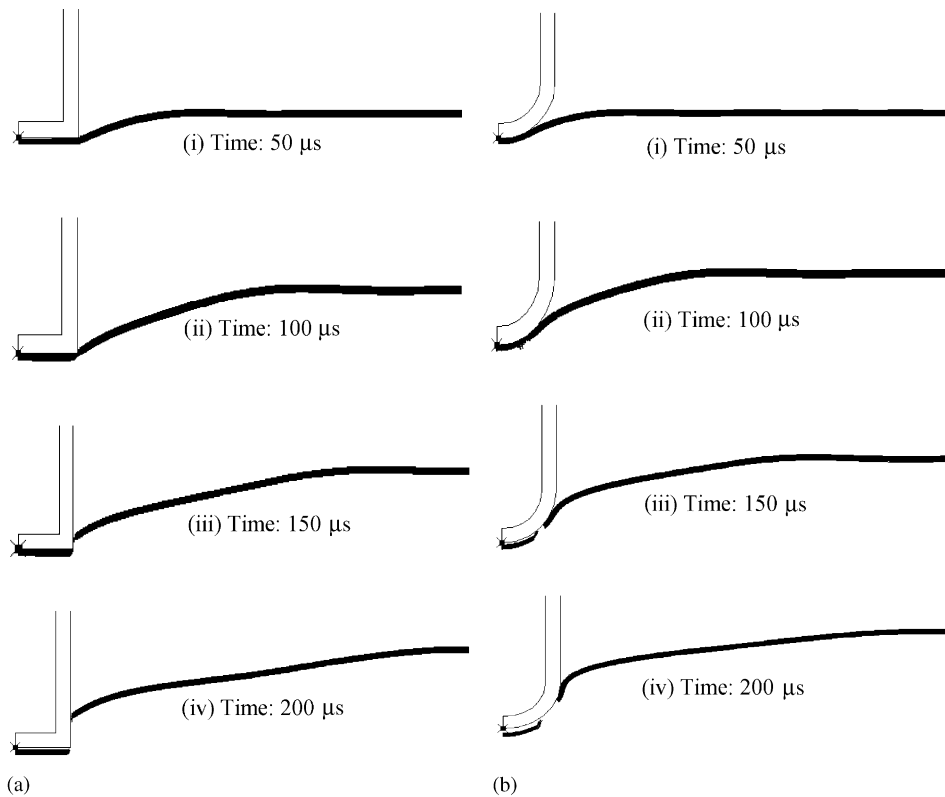


Fig. 14. Predicted progress of deformation of the target plate.

blunt projectile. Values of the maximum deformation of the target plate obtained numerically are listed in Table 5. Actual and predicted deformation profiles of the target plate are compared in Figs. 15 and 16 for blunt and hemispherical projectiles, respectively. Close agreement has been

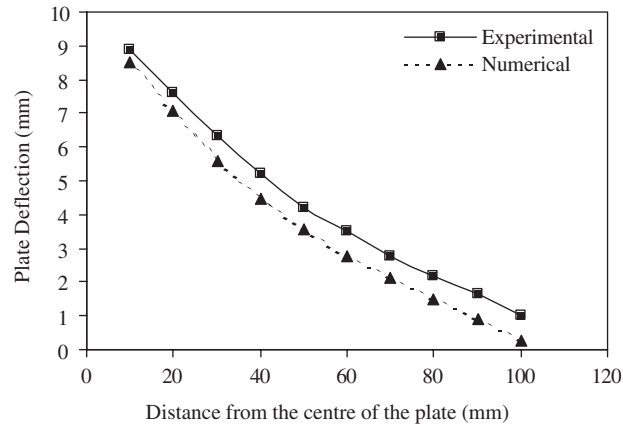


Fig. 15. Deformation profile of the target plate for blunt-nosed projectile case ($V_{\text{imp}} = 115.6$ m/s).

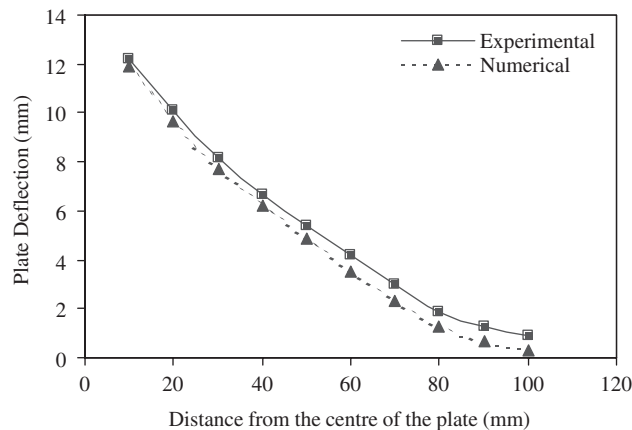


Fig. 16. Deformation profile of the target plate for hemispherical-nosed projectile case ($V_{\text{imp}} = 114.7$ m/s).

found between the actual and predicted pattern of target deformation. It is pertinent to mention that the target plate has been considered as an axisymmetric body for purpose of analysis. However petal formation is observed during actual experiments on impact by hemispherical projectiles (Fig. 3). This failure mode of target plate is not exactly axisymmetric. Numerical results, once petal formation occurs, can only be considered as approximate. Failure of the target plate in case of impact by a blunt projectile is shearing through plug formation. The axisymmetric condition is not violated in this case.

Fig. 17 shows the Von-Mises stress contours in the target plate due to the blunt projectile impact. It is observed that during the initial stages of deformation, largest value of the effective stress is developed at the front side of the target plate in the region where the edge of the projectile contacts the plate. This stress increases with onward movement of the projectile and reaches a peak value at the moment of fracture i.e. when the plug separates from the target. After fracture,

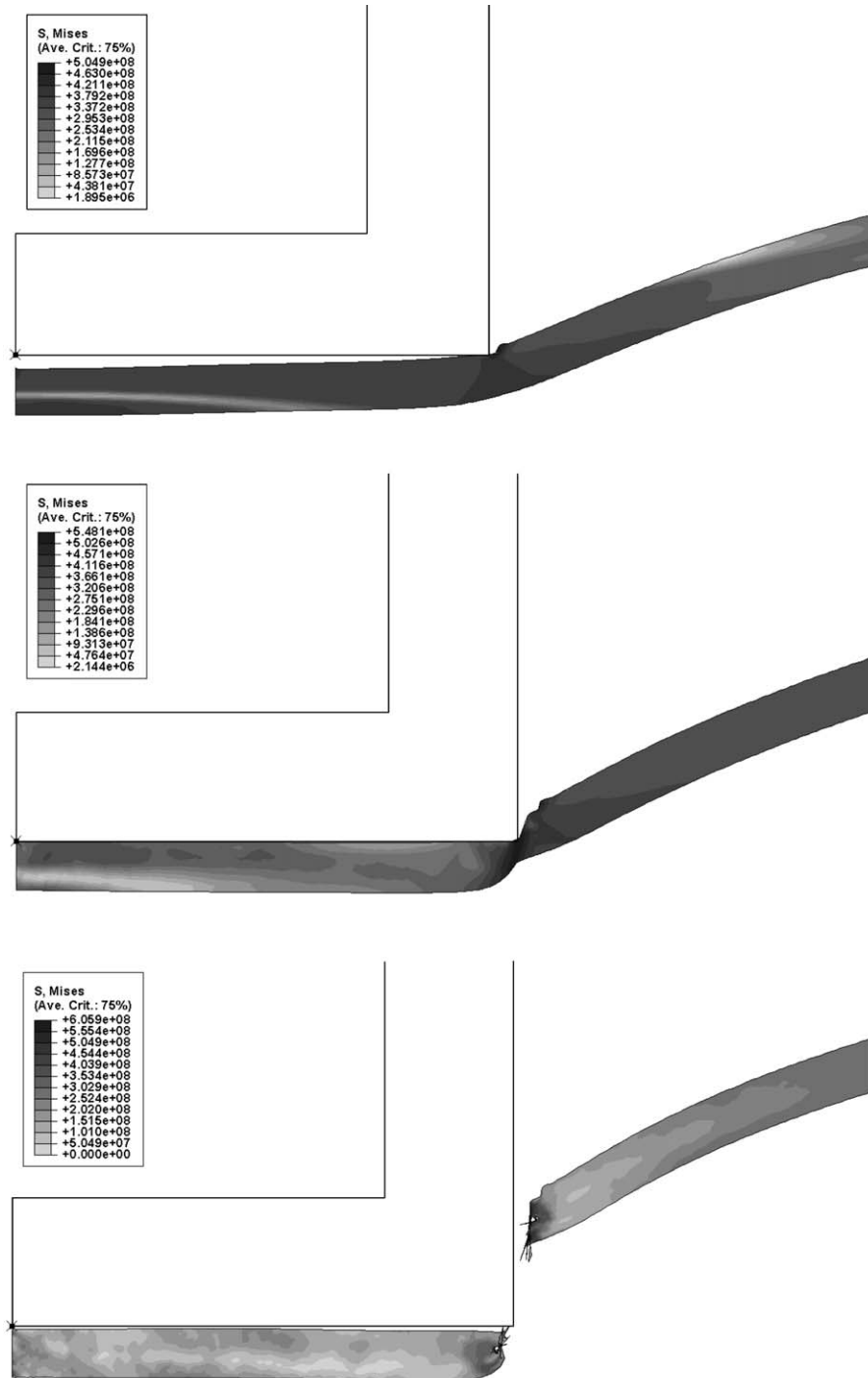


Fig. 17. Predicted Von-Mises stress contours for blunt-nosed projectile case.

the value of the effective stress decreases. Fig. 18 shows the Von-Mises stress contours in the target plate during impact by a hemispherical-nosed projectile. In this case, the target bends when it comes in contact with the projectile. The maximum effective stress is developed in the whole region that is in contact with the projectile. Further movement of projectile causes intense stress localisation or thinning in the contact region. The peak value of stress is reached in the locally stretched region at the time of fracture. The peak value tends to decrease slightly with further movement of the projectile before becoming constant.

Figs. 19 and 20 show the shear stress contours in the target plate due to impact of the two types of the projectile. In case of the blunt projectile, the location of the maximum shear stress in the target plate is the same as that of the Von-Mises stress. Shear stress increases with onward movement of projectile and reaches a maximum value at the instant of fracture or the shearing out of the plug from the target plate. Subsequently the value of the maximum shear stress decreases and becomes almost constant. In the case of the hemispherical-nosed projectile the maximum shear stress occurs in the region of separation of the plug from the target plate. However after the removal of the plug, the value of the maximum shear stress continues to increase in the region of target plate that has been bent due to the projectile impact. The equivalent plastic strain contours in the plate are shown in Figs. 21 and 22 for both projectile cases. It is observed from these figures that the maximum value of the equivalent plastic strain is high in both cases of the projectile, it starts increasing as soon as the projectile comes in contact with the plate and reaches a peak when the plug separates from the plate. After this point the peak value of the plastic strain does not change.

8. Conclusion

1 mm-thick, circular aluminum plates, clamped on the periphery were impacted by projectiles having blunt and hemispherical nose shapes. Initial velocity of the projectile was varied. Impact and residual velocity curves of both types of projectile were measured. Greater velocity drop after impact was observed in case of the hemispherical projectile especially at lower velocities of impact. At impact velocities higher than 100 m/s the curves of velocity drop for both types of the projectile were found to coincide. Blunt-nosed projectiles penetrate the target by removing a circular plug of diameter equal to that of the projectile. Hemispherical projectiles impart greater bending to the target, cause localised thinning and remove a plug from the plate that is smaller in diameter than that of the projectile.

Finite element simulations of the above impact situations were also carried out. It was found that the explicit finite element code ABAQUS in conjunction with the Johnson–Cook material model is capable of simulating the perforation phenomenon fairly accurately.

It was found that the element size is an important parameter affecting the simulation results. The predicted velocity drop of the projectile was found to be close to the actual provided the mesh is sufficiently refined. Adaptive meshing approach was also found to be useful in avoiding excessive distortion of elements and obtaining an economic solution.

Experimental and numerical results were found to agree closely. The maximum difference between experimentally and numerically obtained residual velocities for blunt- and hemispherical-nosed projectiles was 8.7% and 4.5%, respectively. Velocity drop of the projectile was found to

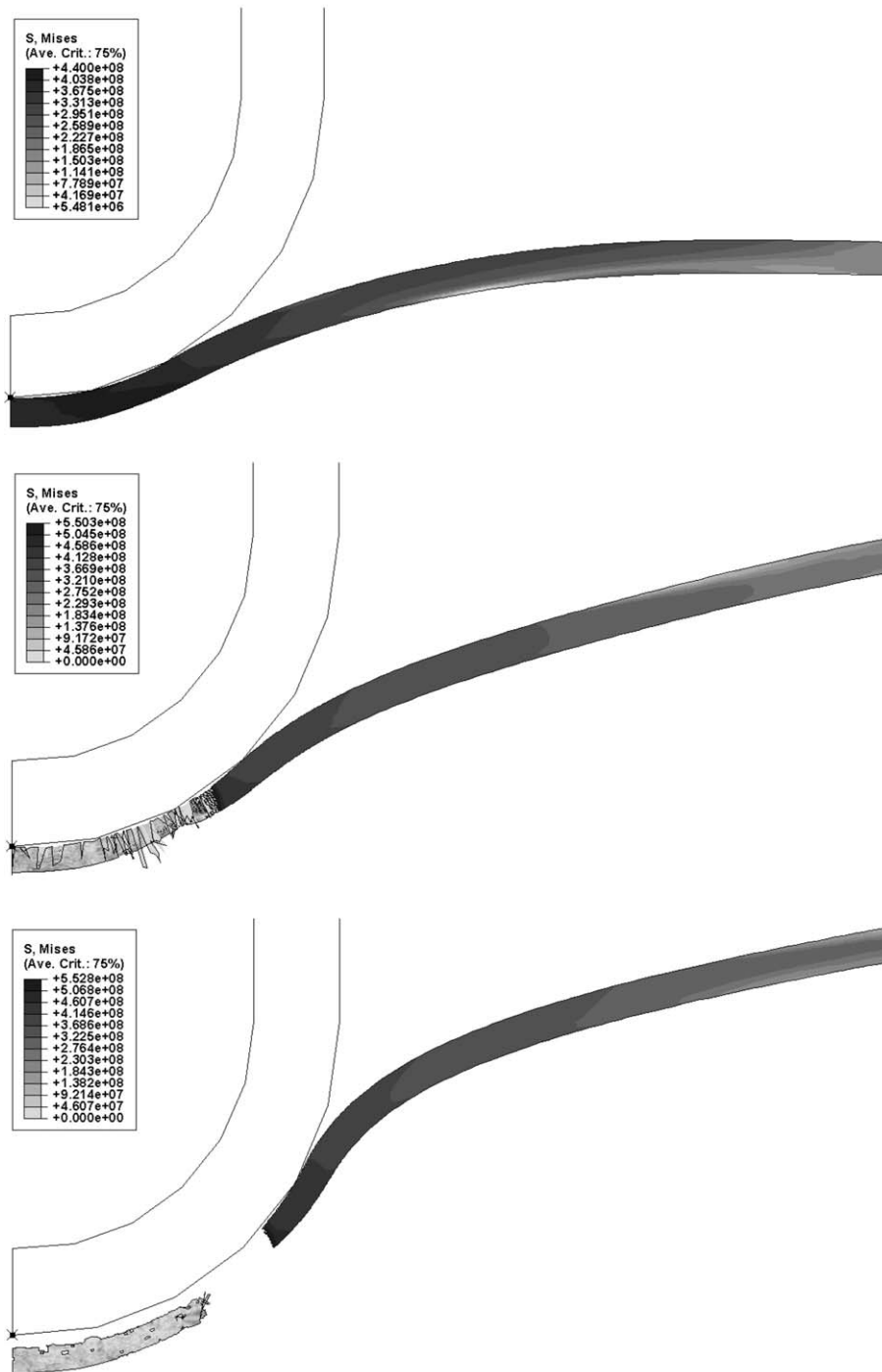


Fig. 18. Predicted Von-Mises stress contours for hemispherical-nosed projectile case.

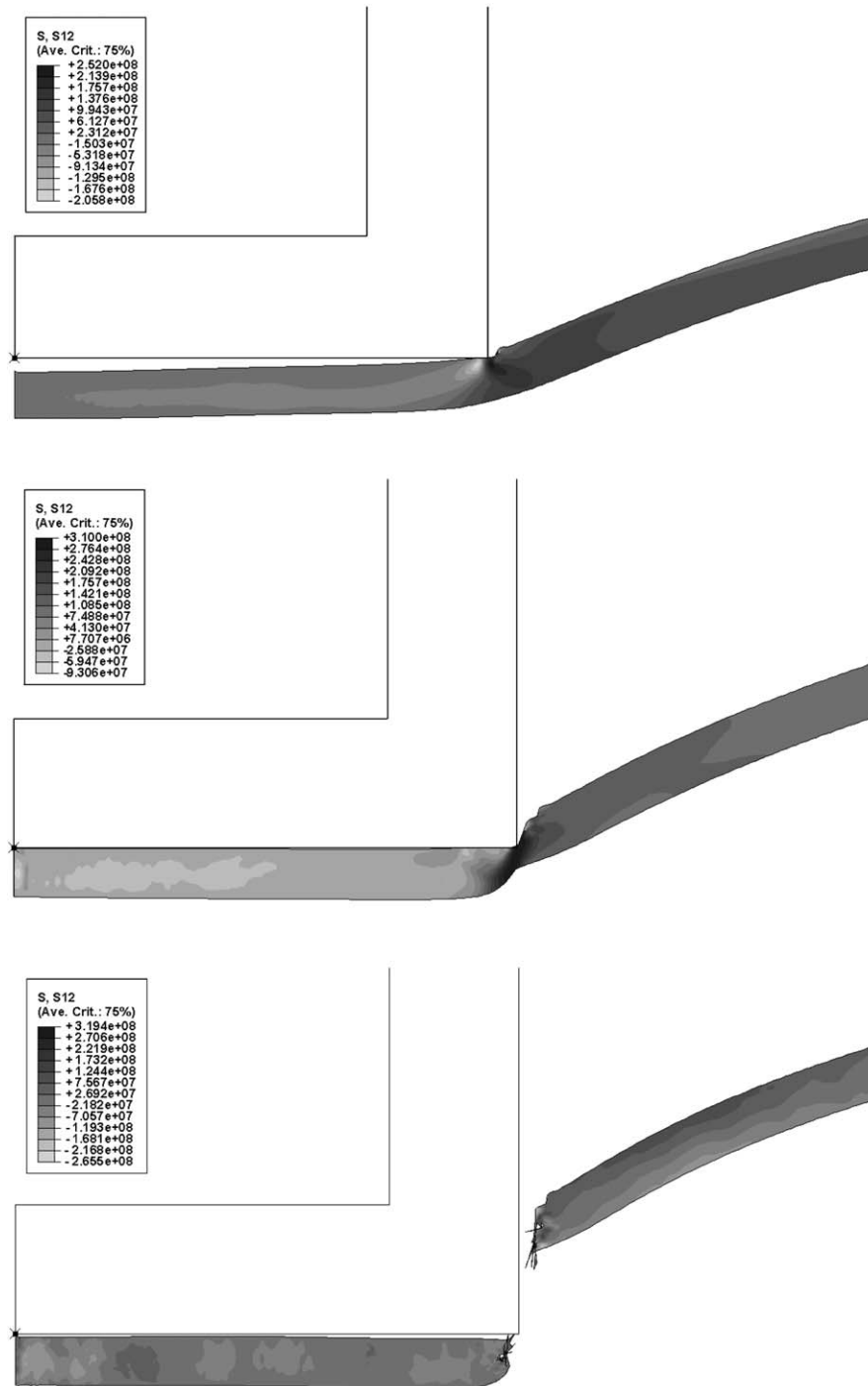


Fig. 19. Predicted shear stress contours for blunt-nosed projectile case.

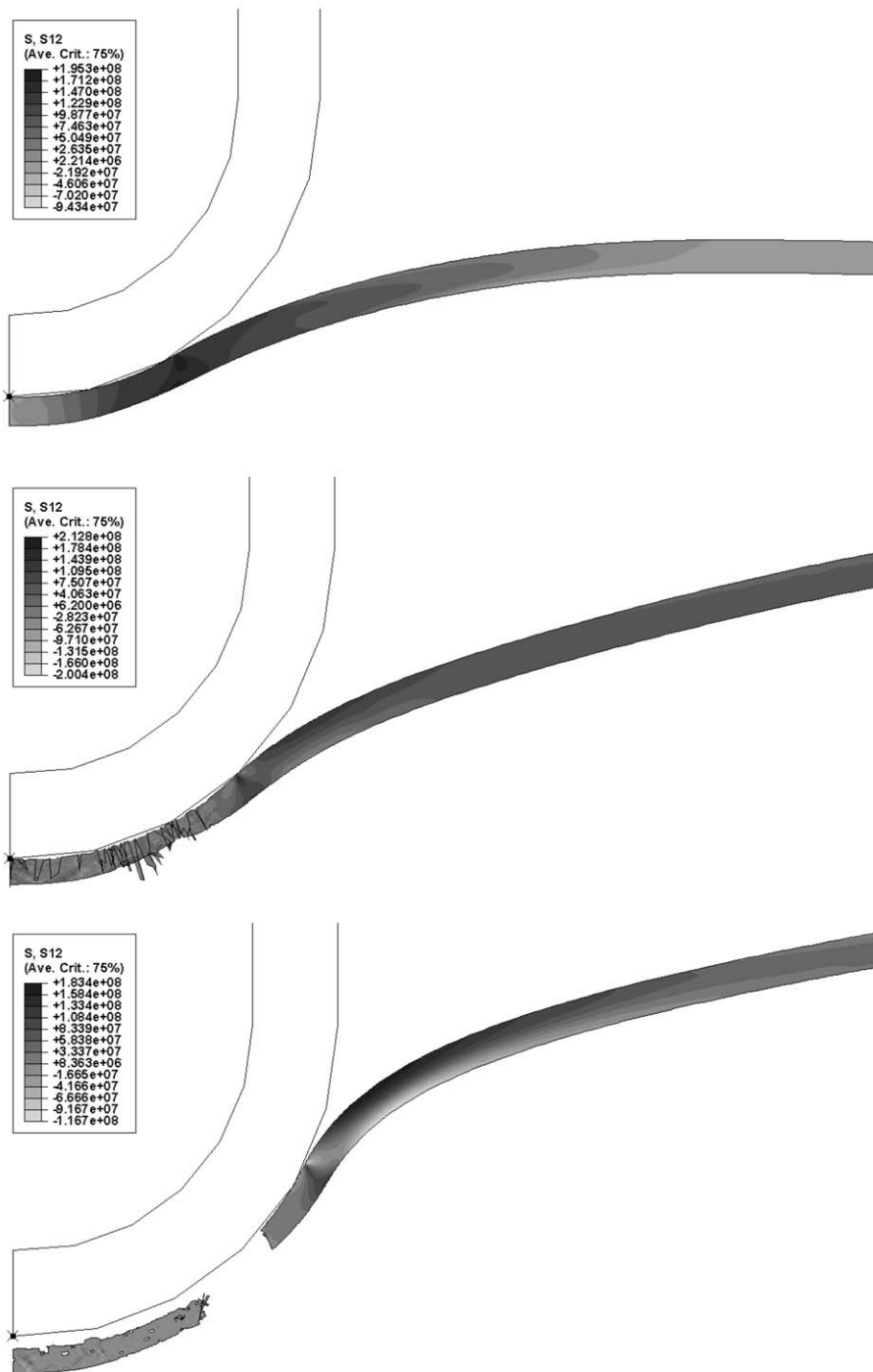


Fig. 20. Predicted shear stress contours for hemispherical-nosed projectile case.

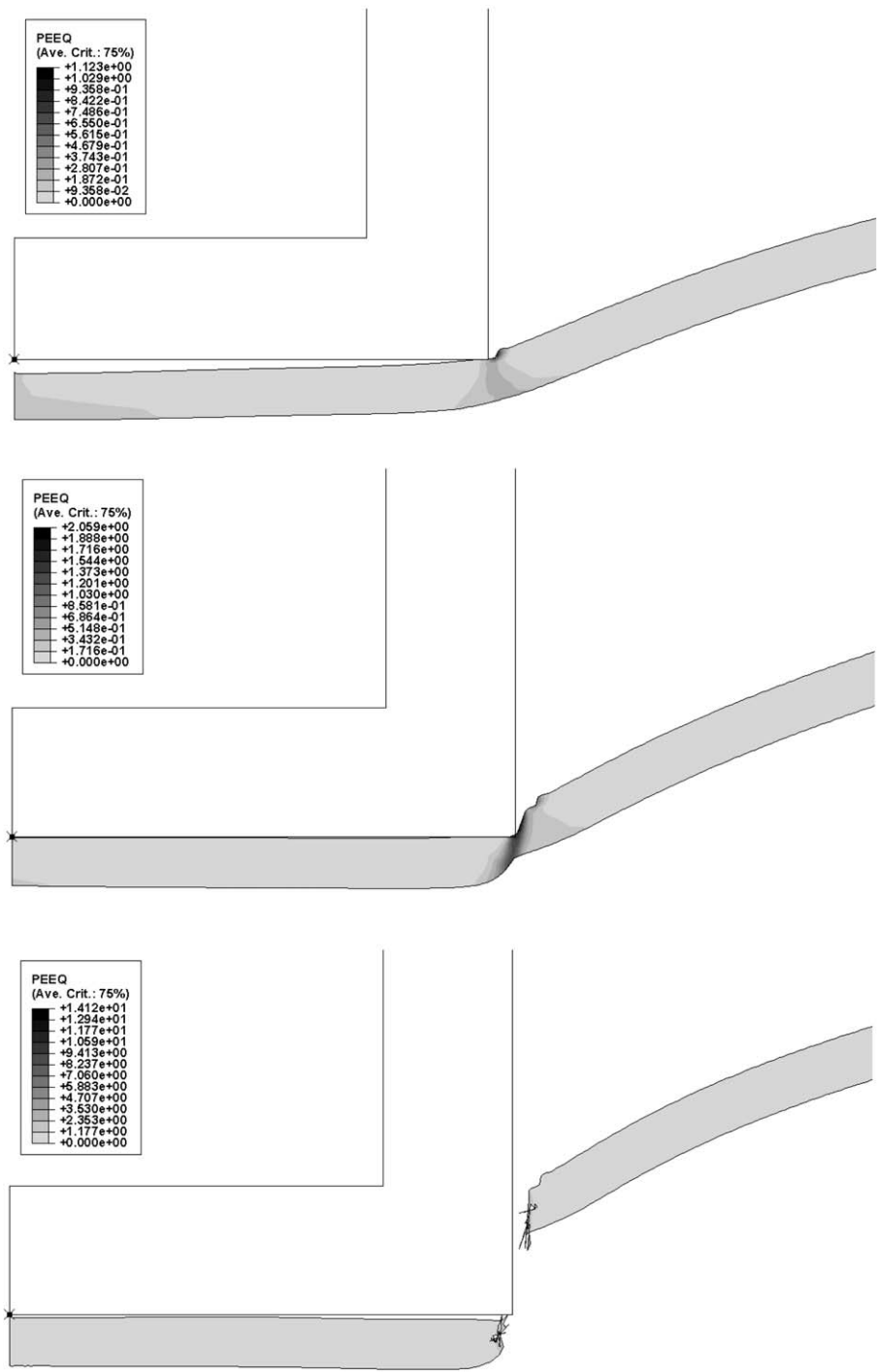


Fig. 21. Predicted contours of equivalent plastic strain for blunt-nosed projectile case.

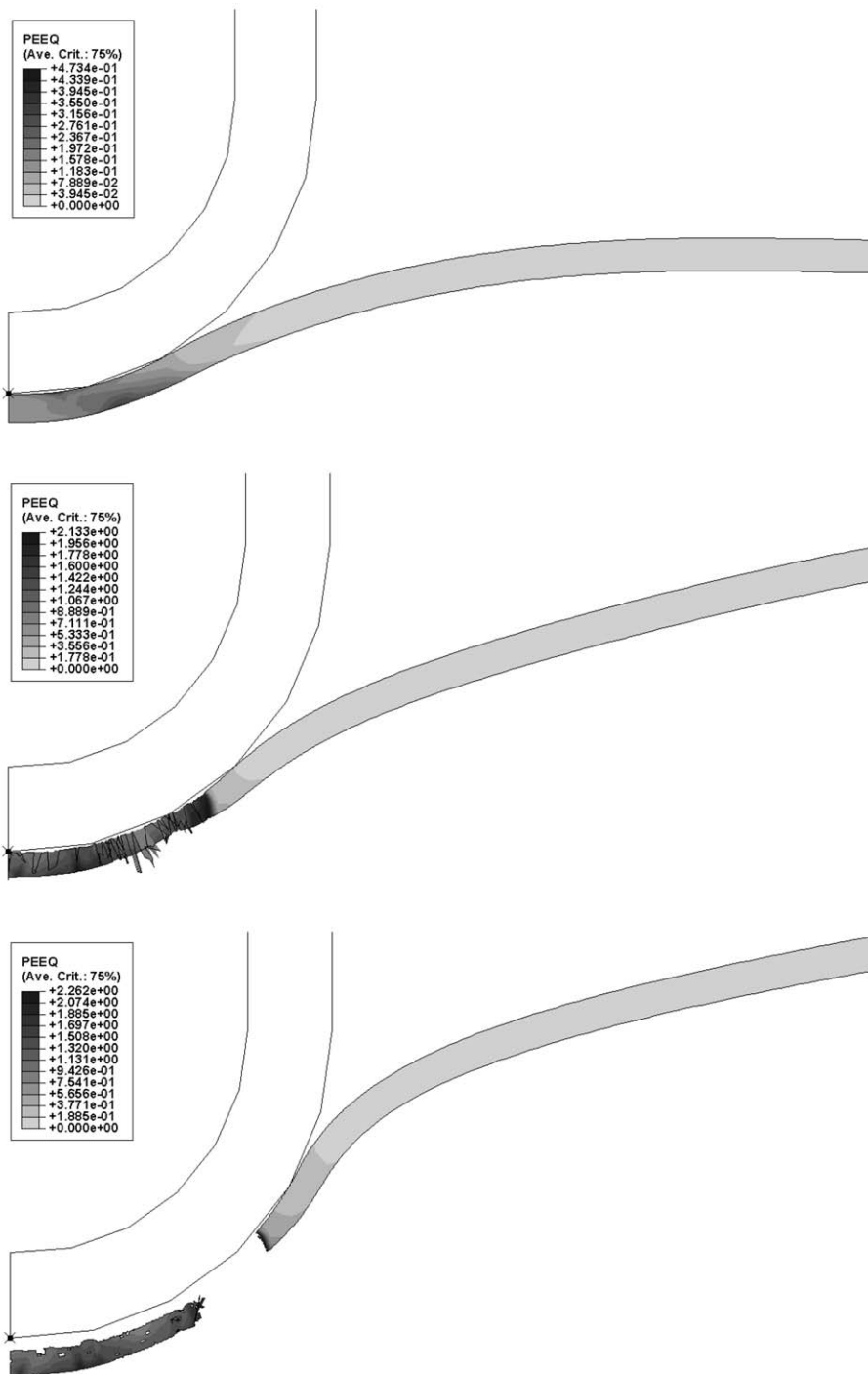


Fig. 22. Predicted contours of equivalent plastic strain for hemispherical-nosed projectile case.

decrease with increase of the impact velocity. Deformation of the target plate was also studied. The degree of plastic deformation was found higher in the hemispherical projectile case. The predicted deformation patterns are in good agreement with the actual in impact by both types of the projectile.

Ballistic limit velocity for both the projectiles was obtained. Higher ballistic limit was found for hemispherical-nosed projectile. Predicted values of the ballistic limit were higher than the actual by 8.2% and 10.7% for blunt and hemispherical projectiles, respectively.

References

- [1] Corran RSJ, Shadbolt PJ, Ruiz C. Impact loading of plates—an experimental investigation. *Int J Impact Eng* 1983;1(1):3–22.
- [2] Levy N, Goldsmith W. Normal impact and perforation of thin plates by hemispherically tipped projectiles—II. Experimental results. *Int J Impact Eng* 1984;2(4):299–324.
- [3] Ipson TW, Recht RF. Ballistic perforation by fragments of arbitrary shape, NWC TP 5927, Denver Research Institute, Naval Weapons Centre, China Lake, CA, USA, 1977.
- [4] Wingrove AL. The influence of projectile geometry on adiabatic shear and target failure. *Metall Trans A* 1973;4:1829–33.
- [5] Othe S, Yoshizawa H, Chiba N, Shida S. Impact strength of steel plates struck by projectiles. *Bull JSME* 1982;25(205):1226–12231.
- [6] Camacho GT, Ortiz M. Adaptive Lagrangian modelling of ballistic penetration of metallic targets. *Comput Meth Appl Mech Eng* 1997;142:269–301.
- [7] Borvik T, Hopperstad OS, Berstad T, Langseth M. Numerical simulation of plugging failure in ballistic penetration. *Int J Solids Struct* 2001;38:6241–64.
- [8] Borvik T, Langseth M, Hopperstad OS, Malo KA. Perforation of 12 mm thick steel plates by 20 mm diameter projectiles with flat, hemispherical and conical noses part I: Experimental study. *Int J Impact Eng* 2002;27:19–35.
- [9] Borvik T, Langseth M, Hopperstad OS, Malo KA. Perforation of 12 mm thick steel plates by 20 mm diameter projectiles with flat, hemispherical and conical noses part II: numerical simulations. *Int J Impact Eng* 2002;27:37–64.
- [10] ABAQUS/Explicit User's Manual. Version 6.3. vol. 1–2. 2002.
- [11] Johnson GR, Cook WH. A constitutive model and data for metals subjected to large strains, high strain rates and high temperatures. In: *Proceedings of the seventh international symposium on ballistics*, The Hague, 1983.
- [12] Johnson GR, Cook WH. Fracture characteristics of three metals subjected to various strains, strain rates, temperatures and pressures. *Eng Fract Mech* 1985;21(1):31–48.
- [13] Bridgman PW. *Studies in large plastic flow and fracture*. New York: McGraw-Hill; 1952.
- [14] Le Roy G, Embury JD, Edwards G, Ashby MF. *Acta Metall* 1981;29:1509.
- [15] Clausen AH, Borvik T, Hopperstad OS, Benallal A. Flow and fracture characteristics of aluminium alloy AA5083–H116 as function of strain rate, temperature and triaxiality. *Mat Sci Eng* 2004;A364:260–72.
- [16] Borvik T, Langseth M, Hopperstad OS, Malo KA. Ballistic penetration of steel plates. *Int J Impact Eng* 1999;22:855–86.